Supporting Information

Ultra-low energy phase change memory with improved thermal stability by tailoring the local structure through Ag doping

Soobin Hwang,[†,‡] Hanjin Park,[§] Dasol Kim,[†,‡] Hyeonwook Lim,[†,‡] Changwoo Lee,[†,‡] Jeong Hwa Han,[†,‡] Young-Kyun Kwon,[§] and Mann-Ho Cho[,†,‡]*

[†]Department of Physics, Yonsei University, Seoul 03722, Republic of Korea

[‡]Atomic Scale Surface Science Center, Yonsei University, Seoul 03722, Republic of Korea

[§]Department of Physics and Research Institute for Basic Sciences, Kyung Hee University, Seoul 02447, Republic of Korea

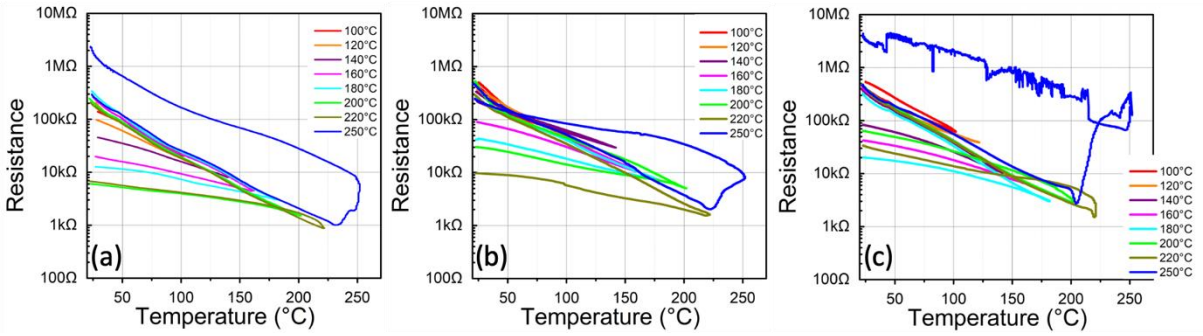

Figure S1. *R–T* curves of Ag-doped Sb_2Te_3 with Ag concentrations of (a) 1.4%, (b) 6%, and (c) 8.2%. The optimal Ag concentration in Sb_2Te_3 is 3.3%.

To determine the optimal amount of Ag dopant for Sb_2Te_3 films, sheet resistance of Ag-doped Sb_2Te_3 films with various compositions of Ag dopants was measured as a function of the annealing temperature. Only 3.3% composition showed stable resistance change until 250 °C, whereas others showed failure after 220 °C. Therefore, analyses for structural evolution and device operation characteristics were performed with 3.3% Ag-doped Sb_2Te_3 film.

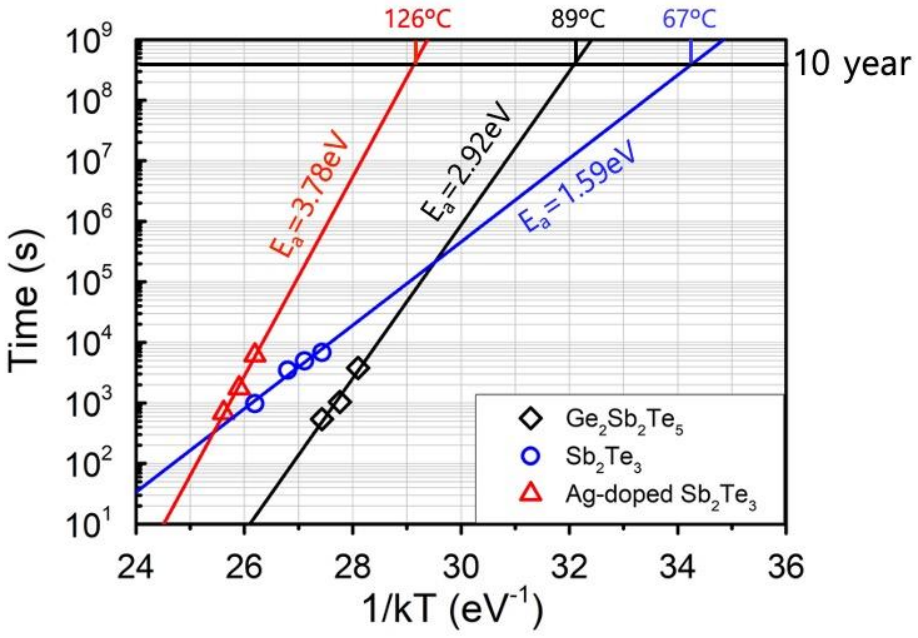

Figure S2. The Arrhenius extrapolation at 10 year of data retention for GST, Sb_2Te_3, and Ag-doped Sb_2Te_3 films.

Data retention properties of GST, Sb_2Te_3, and Ag-doped Sb_2Te_3 are measured to compare thermal stability. Data retention can be determined with failure time of the PCM during isothermal process. Failure time is defined as the time required for the resistance to decrease to half of the initial value at a specific temperature. With the Arrhenius extrapolation of failure time, temperature for 10-year retention ($T_{10\text{-}yr}$) can be achieved. The extrapolated line can be fitted with the Arrhenius equation $t = \tau \exp(E_a/k_B T)$, where t is failure time, τ is proportional time constant, E_a is activation energy, k_B is Boltzmann's constant, and T is specific temperature. As shown in Figure S2, E_a of GST, Sb_2Te_3, and Ag-doped Sb_2Te_3 are 2.92, 1.59, and 3.78 eV, respectively, where $T_{10\text{-}yr}$ of GST, Sb_2Te_3, and Ag-doped Sb_2Te_3 are 89, 67, and 126 °C, respectively. Data retention of Sb_2Te_3 is improved significantly with Ag incorporation in comparison with GST.

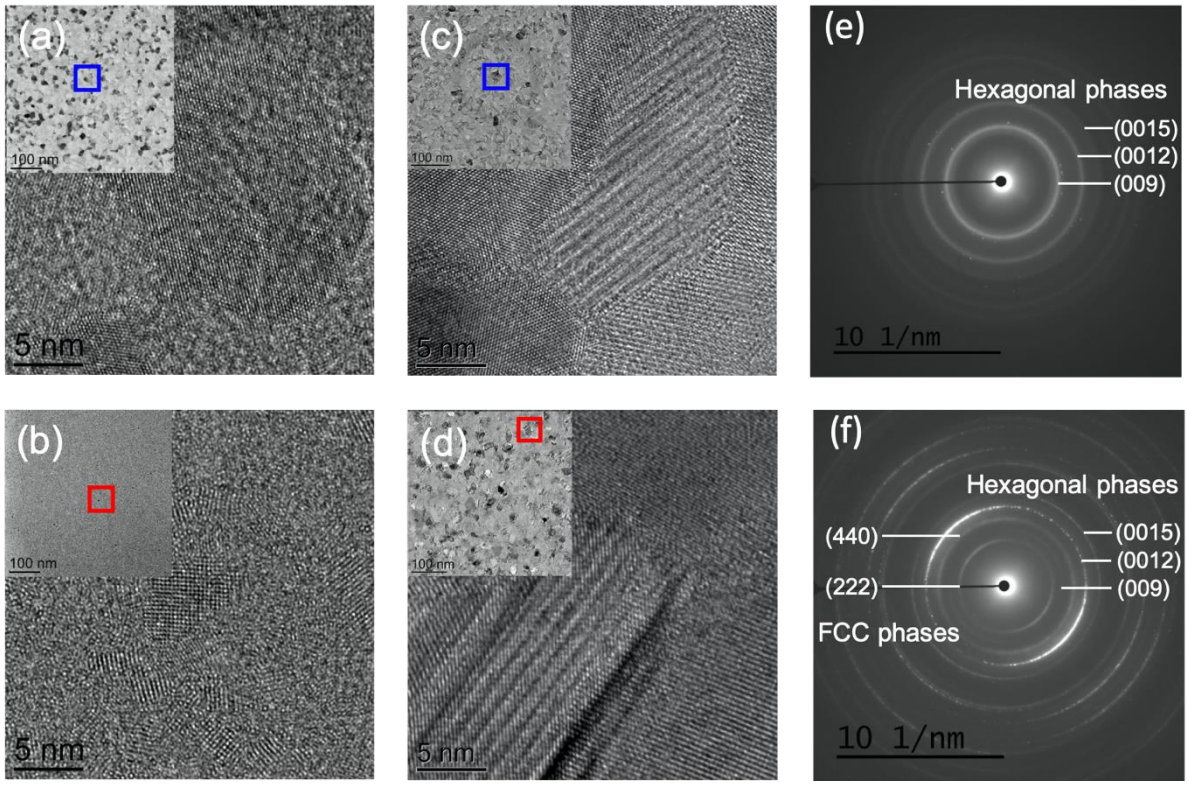

Figure S3. (a-d) HR-TEM images of ~30 nm-thick Sb_2Te_3 films annealed at (a) 140 °C and (c) 200 °C, and Ag-doped Sb_2Te_3 films annealed at (b) 140 °C and (d) 220 °C, confirming the emergence of the FCC and hexagonal phases without any segregation of Ag. The inset images are the corresponding bright-field TEM images. (e-f) SAED patterns corresponding to (c) and (d), respectively.

Transmission electron microscopy (TEM) images and corresponding selected-area electron diffraction (SAED) patterns are measured to investigate the microstructure of Sb_2Te_3 and Ag-doped Sb_2Te_3. As shown in Figure S3 (a) and (b), both Sb_2Te_3 and Ag-doped Sb_2Te_3 films, FCC crystal grains with no Van der Waals gap are observed at annealing temperature of 140 °C. Figure S3 (c) and (d) show the existence of the Van der Waals gap, which is evidence of the hexagonal phase. Figure S3 (e) and (f) show the SAED patterns of corresponding to 220 °C-annealed Sb_2Te_3

and Ag-doped Sb_2Te_3 films, respectively. Only hexagonal phase exists in Sb_2Te_3 film, whereas both the FCC and hexagonal phases exist in Ag-doped Sb_2Te_3 film. This aspect also supports the increase in thermal stability of Sb_2Te_3 with Ag incorporation, where the FCC phase in Ag-doped Sb_2Te_3 stands up to 220 °C, even crystalline phase of Sb_2Te_3 film completely transforms into hexagonal structure.

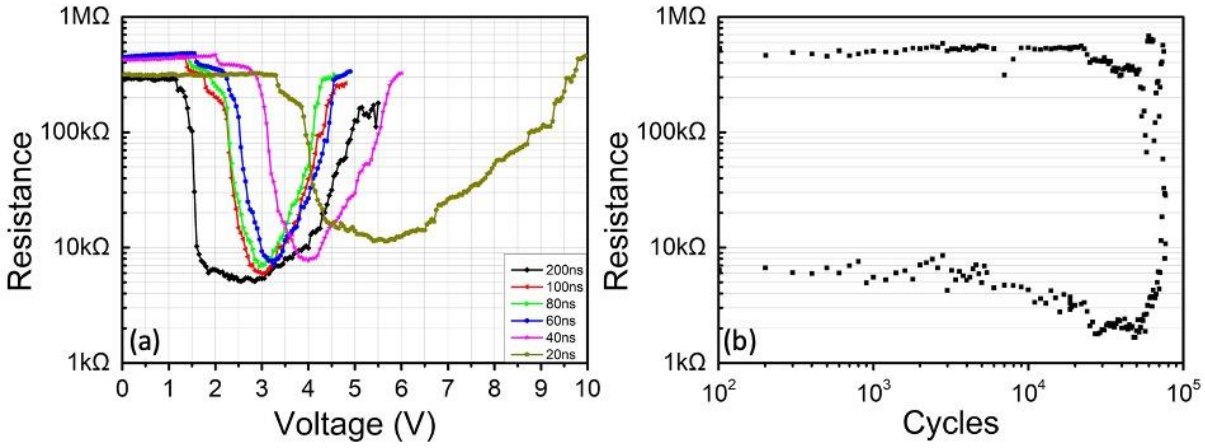

Figure S4. (a) Device operation characteristics and (b) device operation cycles of GST. The SET and RESET states were achieved by applying electrical pulses of width (height) 200 ns (2 V) and 60 ns (2.7 V), respectively.

To compare device operation characteristics of Ag-doped Sb_2Te_3 with standard PCM, device with 320 nm diameter of BEC and 30 nm thickness of GST is fabricated. As shown in Figure S4 (a), 1.15–3.3 V and 3–6.5 V pulses for SET and RESET operation were needed, respectively, changing their width from 200 to 20 ns. Comparing to Sb_2Te_3 and Ag-doped Sb_2Te_3, much higher pulse is required to change the state of GST; therefore, the power consumption of GST is higher than Ag-doped Sb_2Te_3. Moreover, device operation of GST is possible for at least 20 ns, whereas Sb_2Te_3 and Ag-doped Sb_2Te_3 show faster operation speed of 10 ns. The cyclability of Ag-doped Sb_2Te_3

is superior than that of GST (6.0×10^4 cycles), which is lower than the reported value. Generally, cyclability is dependent on the dimension of the device structure, i.e., cyclability of PCM can be increased with increasing thickness of PCM and decreasing the diameter of BEC. Since the reported value was measured at an increased thickness and decreased diameter of BEC in comparison with the device for this study, higher cyclability over 10^5 can be achieved with further scaled device structure.

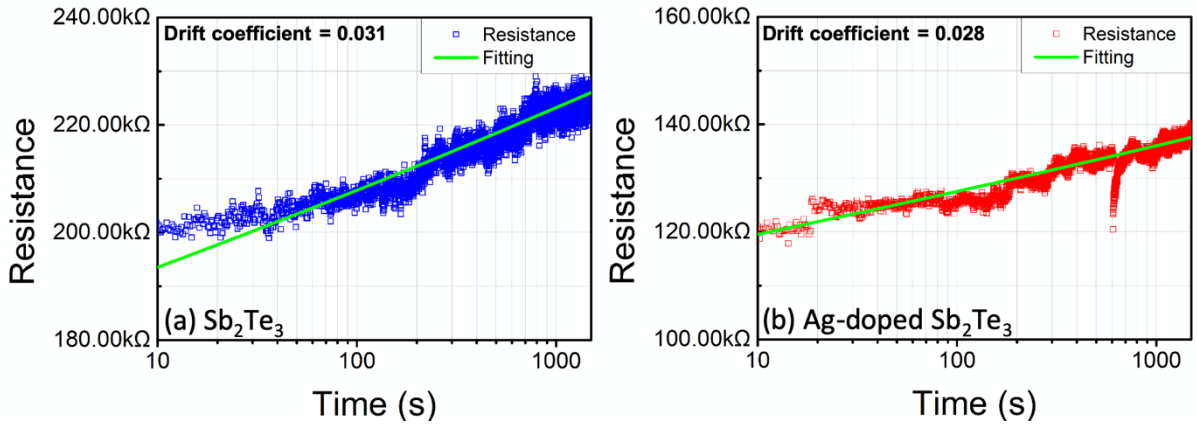

Figure S5. (a-b) Resistance drift characteristics of (a) Sb_2Te_3 and (b) Ag-doped Sb_2Te_3. The drift coefficients are 0.031 and 0.028, respectively.

Evolution of resistance of Sb_2Te_3 and Ag-doped Sb_2Te_3 is measured as function of time to evaluate enhancement in device retention. To quantify the resistance drift characteristics, the resistance-time evolution is fitted with the model $R = R_0\ (t/t_0)^{\nu}$, where R_0 is the resistance at time t_0, t is the time elapsed after t_0, and ν is the drift coefficient. The retention of Sb_2Te_3 device is enhanced by approximately 10% after Ag incorporation.

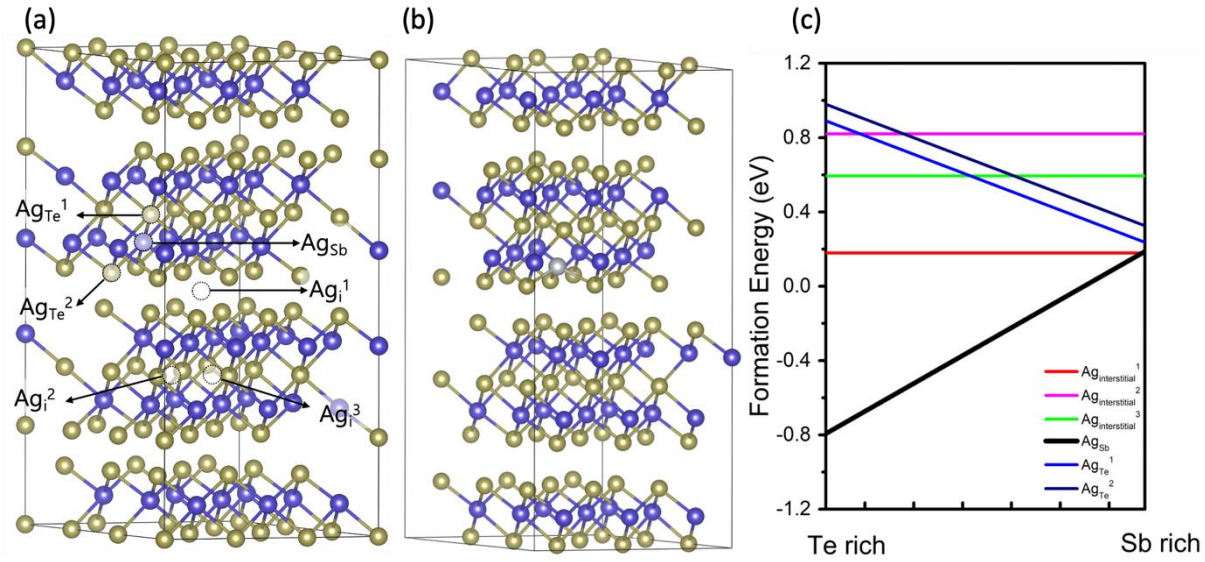

Figure S6. (a) Sb_2Te_3 crystal lattice and possible Ag incorporation sites. $Ag_{Te}^{1,2}$, Ag_{Sb}, and $Ag_{i}^{1,2,3}$ denote two Te substitutions, one Sb substitution, and three interstitial sites, respectively. (b) Ag-doped Sb_2Te_3 crystal lattice with Ag substitution for Sb, which is the most stable structure. (c) Formation energy evolution from Te- to Sb-rich environment for six different configurations. The configuration with Ag replacement of Sb is the most stable for Ag incorporation.

To determine the dopant location, formation energies of the Ag-doped Sb_2Te_3 lattices with various sites were calculated based on density-functional theory. Possible locations for the Ag dopant are confirmed as Sb or Te substitution and interstitial sites. As shown in Figure S6 (c), Ag-doped Sb_2Te_3 lattice becomes the most stable when the dopant substitutes the Sb site. Corresponding crystal lattice is shown in Figure S6 (b).

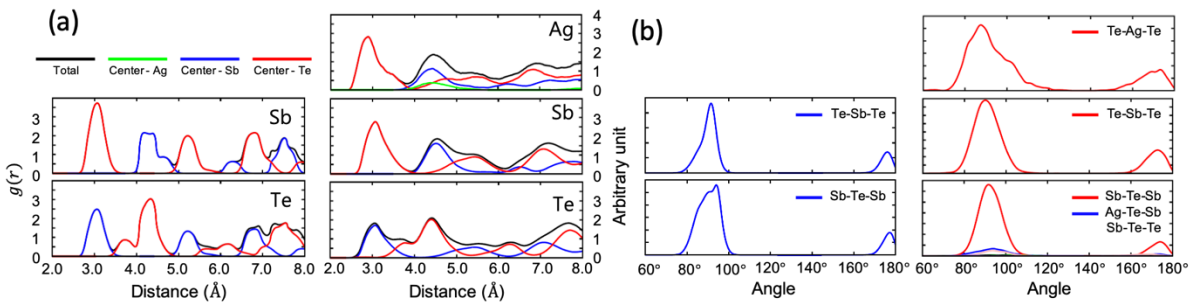

Figure S7. (a) Radial distribution functions (RDFs) and (b) angular distribution functions (ADFs) calculated at 300 K for Sb_2Te_3 (left panels) and Ag-doped Sb_2Te_3 (right panels) using *ab-initio* MD simulations.

To determine changes in bond length and angle of Sb_2Te_3 with Ag incorporation, radial distribution function and angle distribution function are calculated with *ab-initio* MD simulation. The Sb–Te bond length was calculated as 3.07 Å in both Sb_2Te_3 and Ag-doped Sb_2Te_3, which is the average value of the short and long bonds. The peaks for Sb and Te in the RDFs broaden with the Ag incorporation, caused by an increased chemical disorder. The Ag–Te bond length was calculated to be 2.8 Å. The distance from a Te atom to the next nearest atoms increases from 4.3 to 4.5 Å and that to the 3rd nearest atoms from 5.2 to 5.5 Å. The Te–Sb–Te bond angles are distributed around 90° in both Sb_2Te_3 and Ag-doped Sb_2Te_3 indicating that the local structure is an octahedron. However, the Te–Ag–Te bond angle distribution exhibits a shoulder and peak at approximately 105° and 90°, respectively, representing a mixture of tetrahedral and octahedral local structures. Compared to the peak position of the Sb–Te–Sb ADF, the peak of the Ag–Te–Sb ADF shifts slightly to a larger angle, which may be caused by the Ag dopant position located closer to the middle Te atom layer.